International Journal of Heat and Mass Transfer 192 (2022) 122867

Contents lists available at ScienceDirect

International Journal of Heat and Mass Transfer

journal homepage: www.elsevier.com/locate/hmt

Thermal and mass transfer resistance at a liquid-gas interface of an evaporating droplet: A molecular dynamics study

Jesus Gutierrez Plascencia, Eric Bird, Zhi Liang*

Department of Mechanical Engineering, California State University, Fresno, CA 93740, USA

ARTICLE INFO

Article history:
Received 6 January 2022
Revised 7 March 2022
Accepted 27 March 2022

Keywords:
Nanodroplets
Evaporation
Interfacial thermal resistance
Mass transfer resistance
Molecular dynamics

ABSTRACT

Thermal and mass transfer resistance at a liquid-gas interface could strongly affect the evaporation of a micro/nanodroplet. One of the challenges in the investigation of heat and mass transfer across liquid-gas interfaces is that there are two heat transfer modes, namely, evaporation and heat conduction, at an evaporating liquid surface. Interfacial heat conduction was often overlooked in the analysis of evaporation of a liquid droplet. In this work, we derive the analytical expressions for the resistance to the heat and mass flow across a liquid-gas interface of an evaporating droplet from the kinetic theory of gases and verify the theoretical predictions by comparing them to molecular dynamics simulation results. The modeling results show that the temperature jump across the evaporating droplet surface is mainly associated with interfacial heat conduction rather than evaporation, and the vapor density near the liquid-gas interface is determined by the resistance to mass transfer, i.e., evaporation, at the interface. Using the expressions for interfacial thermal and mass transfer resistance, we formulate the temperature jump and vapor density boundary conditions at an evaporating droplet surface and determine the scenario under which the conventional assumptions of continuous temperature profile and saturated vapor at the liquid-gas interface become invalid.

1. Introduction

Evaporation of micro/nanodroplets in a non-condensable gas (NCG) is a process of great importance to a variety of engineering applications such as spray cooling, spray combustion, and superfine inkjet printing [1–4]. Since evaporation occurs on the surface of a liquid, the evaporation rate can be enhanced by increasing the total area of the liquid-gas interface. The total surface area can be significantly increased by splitting a bulk liquid into small droplets. For a given volume of liquid, its total surface area is inversely proportional to the size of droplets. When the droplet size decreases to micro/nanoscale, the finely atomized liquid has a significantly large total surface area, which leads to high evaporation/cooling rates. In this case, the thermal and mass transfer resistance at the liquid-gas interface of droplets could strongly affect the evaporation process. Both experiments and molecular dynamics (MD) simulations have shown the existence of a temperature jump at the evaporating liquid-gas interface of micro/nanodroplets [5–10]. This jump in temperature indicates that the conventional assumption of a continuous temperature profile across the liquid-gas interface [11] is inaccurate or even invalid for micro/nanodroplets. Moreover, in hydrodynamic modeling of evaporation processes, it is often assumed that the vapor in the vicinity of a liquid-gas interface is saturated and transferred from the nanodroplet surface to the ambient gas through mass diffusion/convection [11–13]. However, recent experimental and MD studies show that vapor density near a fast-evaporating surface is well below the saturated vapor density evaluated at the liquid surface temperature [14–18]. All these results indicate that the conventional assumption of thermodynamic equilibrium at the liquid-gas interface could be invalid for the analysis of evaporation of micro/nanodroplets.

Evaporation of a liquid droplet in a NCG is a non-equilibrium process. The heat and mass transfer at an evaporating droplet surface is driven by the temperature jump across the liquid-gas interface and unsaturated vapor near the droplet surface. In hydrodynamic modeling of evaporation of nanodroplets, it was shown that applying the thermodynamic equilibrium boundary conditions could result in significant overestimate of the evaporation rate [10,19]. To specify appropriate temperature jump and vapor density boundary conditions on the surface of evaporating micro/nanodroplets, it is essential to fundamentally understand the heat and mass transfer mechanisms at the surface of a droplet and develop a theoretical model to predict the resistance to the heat and mass transfer across the liquid-gas interface. Understanding

* Corresponding author.
E-mail address: zliang@csufresno.edu (Z. Liang).

https://doi.org/10.1016/j.ijheatmasstransfer.2022.122867
0017-9310/

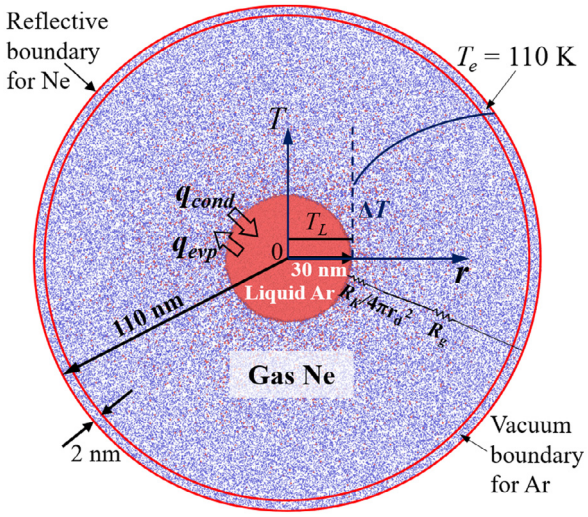

Fig. 1. A snapshot of the model system and schematics of NEMD simulation setups. Red and blue dots represent Ar and Ne atoms, respectively.

heat and mass transfer at an evaporating surface requires treatment from the kinetic theory of gases (KTG). In this work, we use the KTG to study the heat and mass transfer mechanisms at an evaporating nanodroplet surface. Based on the KTG, we derive analytical expressions for the thermal and mass transfer resistance at a liquid-gas interface. To validate the theoretical predictions of interfacial thermal and mass transfer resistance, one needs to measure the temperature and density of vapor and NCG near the droplet surface, and the mass and thermal accommodation coefficients at the liquid-gas interface accurately. Experimental quantification of these properties is currently challenging [7]. Hence, in this work we resort to MD simulations, which can readily determine all the quantities in the theoretical model, to validate the predictions from the KTG. The analytical expressions for the thermal and mass transfer resistance at a liquid-gas interface will allow us to formulate temperature and density boundary conditions for continuum modeling of an evaporating micro/nanodroplet in a NCG.

In the next section, we introduce the heat and mass transfer mechanism across the liquid-gas interface of an evaporating droplet and the analytical expressions of interfacial thermal and mass transfer resistance derived from the KTG. In Section 3, we describe the MD model used to validate the theoretical predictions. The simulation results are shown in Section 4. In Section 5, we discuss how the interfacial thermal and mass resistance will affect the evaporation of micro/nanodroplets and the conditions under which the conventional assumptions of continuous temperature profile and saturated vapor at the liquid-gas interface become invalid. Finally, we close with conclusions.

2. Theory

2.1. Heat transfer mechanism

As depicted in Fig. 1, we consider a model system containing a liquid nanodroplet evaporating in a NCG. There are two heat transfer modes at the liquid-gas interface of the droplet. The first mode is the evaporation of the liquid droplet mainly driven by the density difference $\Delta\rho = \rho_{sat}(T_L) - \rho_v$, where $\rho_{sat}(T_L)$ is the saturated vapor density evaluated at the liquid surface temperature T_L, and ρ_v is the density of vapor near the droplet surface. If ρ_v in the surrounding gas phase is lower than $\rho_{sat}(T_L)$, evaporation occurs. The evaporation heat flux, q_{evp}, leads to the cooling of the droplet. As the droplet temperature reduces, the temperature difference between the surrounding NCG and the liquid droplet results in the second heat transfer mode, i.e., heat conduction from the surrounding gas to the droplet, which increases the droplet temperature. As shown in Fig. 1, droplet heating and evaporation processes occur simultaneously at the droplet surface and the interfacial heat conduction flux (q_{cond}) is in the opposite direction of q_{evp}.

If q_{evp} is higher than q_{cond}, the droplet temperature will decrease. The decrease of the droplet temperature will lead to the decrease in $\rho_{sat}(T_L)$, which in turn reduces q_{evp}. On the other hand, the decrease of the droplet temperature increases the temperature difference between the surrounding NCG and the liquid droplet, which leads to a higher q_{cond}. As q_{evp} decreases and q_{cond} increases, eventually the energy balance ($q_{evp} = q_{cond}$) at the liquid-gas interface will be achieved. If q_{evp} is initially lower than q_{cond}, using a similar analysis one can see that the energy balance at the liquid-gas interface will also be eventually established. When $q_{evp} = q_{cond}$, the evaporation of the droplet in a NCG will be in a quasi-steady state (QSS), and the droplet temperature will remain almost constant [8].

2.2. Interfacial thermal resistance

We first study the temperature jump, ΔT, across the liquid-gas interface. It is well known that heat flow across an interface will result in a temperature jump, ΔT, across the interface due to the presence of interfacial thermal resistance (also known as Kapitza resistance [20], R_K). R_K is defined as

$$R_K = \Delta T/q, \tag{1}$$

where q is the heat flux across the interface. As we discussed in Section 2.1, there are two heat transfer modes, namely, evaporation and heat conduction, at an evaporating liquid surface. Both experimental and MD studies find that the gas temperature near the surface of evaporating micro/nanodroplets is higher than the droplet temperature [5–10]. This indicates the measured ΔT is in the same direction as q_{cond}. Furthermore, if considering only heat transfer by evaporation at the droplet surface, ΔT predicted by the KTG would be orders of magnitude smaller than the measured value and in the opposite direction [9,21]. All these results imply that ΔT across the liquid-gas interface is associated with interfacial heat conduction (i.e., heat exchange by collisions between gas molecules and the liquid surface) rather than evaporation. The KTG predicts that the resistance to heat conduction across a liquid-gas interface is determined by [18,22,23]

$$1/R_K = N_g\left(c_V + \frac{1}{2}R\right)\cdot 2\alpha_T/(2-\alpha_T), \tag{2}$$

where c_V is the constant-volume specific heat of gas near the liquid-gas interface and R is the universal gas constant. N_g in Eq. (2) is the liquid-gas collision rate per unit area. For incident gas molecules with an average temperature, T_g, and a density, ρ_g, N_g is given by [22]

$$N_g = \rho_g\sqrt{RT_g/2\pi M_g}, \tag{3}$$

where M_g is the molar mass of gas. In Eq. (2), α_T is the thermal accommodation coefficient which quantifies the heat exchange efficiency at a liquid-gas interface and is defined as

$$\alpha_T = (E_r - E_i)/(E_s - E_i), \tag{4}$$

where E_i and E_r are the average energy of incident and reflected gas molecules, respectively, and E_s is the average energy a gas would carry if it equilibrated with the liquid surface upon reflection. Eqs. (2) and (3) indicate that increasing the gas density ρ_g

will increase the liquid-gas collision rate which makes the heat exchange between liquid and gas more efficient, thus reducing the interfacial conduction resistance R_K which leads to a smaller ΔT for a given heat flux. This theoretical prediction agrees qualitatively with the findings in recent MD studies of evaporation of nanodroplets [8–10]. Hence, it further shows that ΔT at the evaporating droplet surface is associated with interfacial heat conduction. In this work, we will carry out MD simulations of nanodroplet evaporation in a NCG to test the accuracy of Eq. (2) in the prediction of R_K at the liquid-gas interface.

2.3. Interfacial resistance to mass transfer

Now we study the density difference $\Delta\rho = \rho_{sat}(T_L) - \rho_v$ at the evaporating droplet surface. The KTG predicts that $\Delta\rho$ is a driving force for evaporation which results in an evaporation flux, J_{evp}, across the liquid-gas interface. Similar to the definition of interfacial thermal resistance R_K in Eq. (1), we can define the mass transfer resistance, R_M, at the evaporating surface by

$$R_M = \Delta\rho / J_{evp}. \tag{5}$$

Based on the KTG, we now derive an analytical expression for R_M. A well-known equation that is derived from the KTG and widely used to model the evaporation process is the Schrage equation [7]:

$$J_{evp} = \frac{2\alpha_M}{2-\alpha_M}\sqrt{\frac{R}{2\pi M_v}}\left[\rho_{sat}(T_L)\sqrt{T_L} - \rho_v\sqrt{T_v}\right], \tag{6}$$

where T_v and ρ_v are the temperature and density of the vapor adjacent to the liquid-gas interface, respectively. Here the vapor refers to the fluid undergoing phase change at the liquid-gas interface instead of the NCG. In Eq. (6), M_v and α_M are the molar mass and the mass accommodation coefficient of the fluid undergoing phase change. α_M is defined as the fraction of vapor molecules that strike the interface and are accommodated to the liquid phase. When evaporation occurs, vapor molecules will leave the liquid surface with a macroscopic velocity. Therefore, R_M at an evaporating surface is an interfacial mass convection resistance. Once the liquid changes into vapor at the liquid-gas interface, the vapor near the interface is transferred to the surrounding NCG through mass diffusion if we assume a stagnant NCG.

Recent experimental and MD studies [14–18] show that the evaporation flux, J_{evp}, can be well predicted by the Schrage equation. Hence, we derive the analytical expression for R_M from Eq. (6). Assuming the vapor temperature T_v and the NCG temperature T_g are the same near the interface, we have $\Delta T = T_v - T_L$. Substituting this relation and $\Delta\rho = \rho_{sat}(T_L) - \rho_v$ into Eq. (6), we obtain

$$J_{evp} = \frac{2\alpha_M}{2-\alpha_M}\sqrt{\frac{RT_L}{2\pi M_v}}\left[\rho_{sat} - (\rho_{sat} - \Delta\rho)\sqrt{1+\frac{\Delta T}{T_L}}\right]. \tag{7}$$

Assuming small $\Delta T/T_L$, we expand the square root in the square bracket of Eq. (7) and neglect high order terms, obtaining the following:

$$J_{evp} \approx \frac{2\alpha_M}{2-\alpha_M}\sqrt{\frac{RT_L}{2\pi M_v}}\rho_{sat}\left[\frac{\Delta\rho}{\rho_{sat}} - \frac{\Delta T}{2T_L} + \frac{\Delta\rho}{\rho_{sat}}\frac{\Delta T}{2T_L}\right]. \tag{8}$$

From Eq. (1), we know $\Delta T = q_{cond}R_K$. At QSS, $q_{cond} = q_{evp} = J_{evp}h_{fg}$, where h_{fg} is the latent heat of vaporization of the model fluid undergoing phase-change. Hence, we have the relation $\Delta T = J_{evp}h_{fg}R_K$. After substituting this relation into Eq. (8), neglecting the high order term (i.e., the last term in the square bracket) in Eq. (8), and manipulating the resulting equation, we obtain the analytical expression for R_M

$$R_M = \frac{\Delta\rho}{J_{evp}} = \frac{2-\alpha_M}{2\alpha_M}\sqrt{\frac{2\pi M_v}{RT_L}} + \frac{\rho_{sat}h_{fg}R_K}{2T_L}. \tag{9}$$

The Schrage equation (i.e., Eq. (6)) indicates that the evaporation flux J_{evp} is affected by both the density difference $\Delta\rho = \rho_{sat}(T_L) - \rho_v$ and the temperature difference $\Delta T = T_v - T_L$. As Eq. (9) is derived from the Schrage equation, it is reasonable to find in Eq. (9) that the mass transfer resistance R_M at the liquid-gas interface of an evaporating droplet depends on both the liquid surface temperature T_L and the interfacial thermal resistance R_K. If Eqs. (2) and (9) give accurate predictions of R_K and R_M, they could then be used to formulate temperature jump and density boundary conditions for continuum modeling of droplet evaporation in a NCG.

3. MD simulations of nanodroplet evaporation in a NCG

3.1. The MD model system

To test the accuracy of Eqs. (2) and (9), we carry out MD simulations of evaporation of a model liquid Ar nanodroplet in a non-condensable Ne gas. As shown in Fig. 1, we locate the model Ar nanodroplet at the center of a spherical region whose radius is constant at $r_g = 110$ nm. A reflective boundary condition is applied to specularly reflect all fluid molecules that impact the spherical boundary. The model system initially contains about 2.3 million Ar atoms in the nanodroplet and 2 million Ne atoms in the surrounding gas. The initial radius of the droplet is around 30 nm so that the curvature effects on model fluid properties such as α_M and ρ_{sat} can nearly be ignored [24–26].

All interatomic interactions for the model fluids are described by the truncated and shifted Lennard-Jones (LJ) potential with parameters given in Table 1 [26,27]. The cutoff distance for all LJ interactions is 10.9 Å. We use the velocity Verlet algorithm [28] with a time step size of 8 fs to integrate the equations of motions. To reach a QSS evaporation of the model nanodroplet, one needs to run the MD simulation for several tens of ns. The Ar-Ne model system whose interatomic potential can be well described by the simple LJ potential allows us to carry out MD simulations in a system containing several million atoms for several tens of ns. In this work, all MD simulations are performed using the LAMMPS simulation package which has a high parallel efficiency for LJ fluids [29].

Table 1
The LJ parameters used in the MD simulations.

	Ar-Ar [27]	Ne-Ne [27]	Ar-Ne [26]	Au-Ar [26]	Au-Ne [26]
ϵ (meV)	10.3	4.05	4.05	10.3	4.05
σ (Å)	3.41	2.72	3.41	3.17	3.17

3.2. Simulation procedure

In the MD simulation, positions of atoms are adjusted every time step to constrain the center of mass of the model system at the center of the simulation cell to prevent the nanodroplet from drifting. We first equilibrate the model system at a temperature of 80 K using the Berendsen thermostat [30]. At thermal equilibrium, the model Ar droplet is surrounded by a Ne-Ar gas mixture with a Ne partial pressure $P_{Ne} = 4$ atm. To mimic the process of heating and evaporation of a liquid nanodroplet, we then turn off the thermostat and set a spherical shell of 2 nm thickness located at the edge of the spherical simulation region as a heat reservoir. The temperature of the heat reservoir is maintained at $T_e = 110$ K by

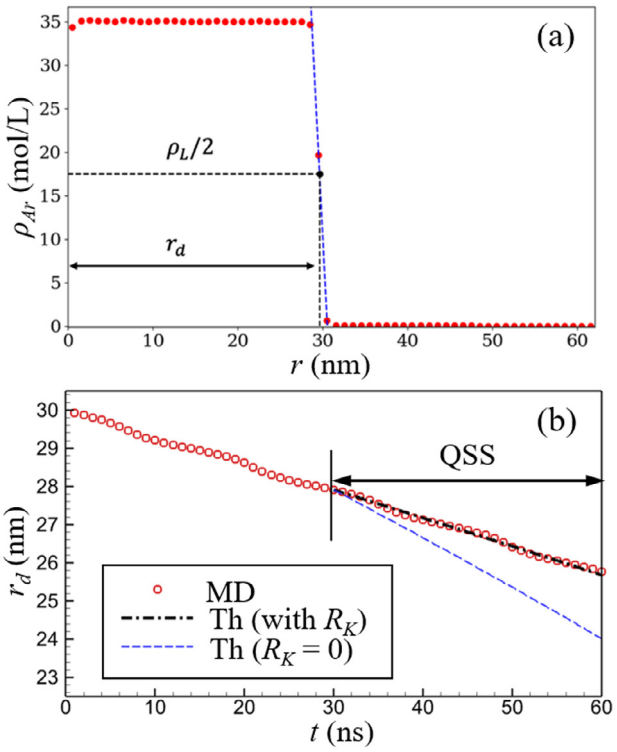

Fig. 2. (a) The schematic represents the method used to determine the position of r_d from the radial density profile. (b) Time evolution of droplet radius r_d in the case of initial $P_{Ne} = 4$ atm and $r_g = 110$ nm. The dashed line is the theoretical prediction from Eq. (14) with R_K determined from the MD simulation. The solid line is the prediction from Eq. (14) with $R_K = 0$.

the velocity rescaling of Ne molecules in the heat reservoir at each time step. Meanwhile, we eliminate all Ar molecules which entered or are situated inside the heat reservoir to mimic the evaporation of Ar molecules into a gas environment with zero Ar concentration far from the droplet. With this simulation setup, heat conduction from the gas to the droplet and evaporation from the droplet to the gas occur simultaneously in the model system. After the aforementioned non-equilibrium MD (NEMD) simulation is carried out for 30 ns, a QSS is reached, and the change in droplet temperature becomes negligible as time progresses. Subsequently, the NEMD simulation is carried out for another 30 ns for data averaging.

In the NEMD simulation, we divide the system into 110 bins in the radial direction. The thickness of each bin is 1 nm. A density profile of Ar along the radial direction of the system is recorded periodically every 0.1 ns. With these profiles, we track the location of r_d by fitting a linear function between the last data point where the density is higher than half the average liquid density, $\rho_L/2$, and the first data point where the density is less than $\rho_L/2$, as depicted in Fig. 2(a). With this linear fit, the location of r_d is determined by finding the value of r where the density is equal to $\rho_L/2$. In the recent MD simulations of evaporation of a LJ fluid and a polymer, it was shown that at an evaporating liquid surface the isotropic temperature profile splits into an anisotropic temperature profile at the position where the fluid density is roughly $\rho_L/2$ [31,32]. In our recent MD studies, we tested the accuracy of Schrage equation in the prediction of the evaporation rate of monatomic LJ fluid [15], polymer [18], and water [33]. In all cases studied, we found Schrage equation with T_L evaluated at the position where the fluid density is $\rho_L/2$ gives accurate prediction of the evaporation rate. Hence, it is reasonable to define the liquid surface at the position where the fluid density is equal to $\rho_L/2$. By applying this method at every obtained density profile, we obtain the time evolution of the droplet size as shown in Fig. 2(b).

The fluid temperature and density profiles are obtained directly from the NEMD simulation by dividing the system into 1 nm thick radial bins and averaging the fluid properties in each bin during the QSS period. The fluid's radial direction macroscopic velocity is subtracted in each bin when calculating the fluid temperature. We determine the average molar flow rate $\dot{M}_{Ar}$ in each bin using

$$\dot{M}_{Ar} = \sum_{i=1}^{N} v_{r,i}/N_A \Delta r, \tag{10}$$

where N is the number of Ar atoms in each bin, N_A is Avogadro's number, $v_{r,i}$ is the radial velocity of Ar atom i, and Δr is the thickness of each bin. To obtain better statistics of all fluid properties in the gas phase, we divide the gas region between $r = 28$ nm and $r = 100$ nm into eight bins of equal thickness and calculate the average gas properties in each bin. From the NEMD simulation results, we will directly determine R_K and R_M using their definitions given by Eqs. (1) and (5), respectively, and verify the KTG predictions given by Eqs. (2) and (9).

3.3. Determination of fluid properties

To obtain the theoretical predictions of R_K and R_M from Eqs. (2) and (9), we need to know α_T of Ne gas on a liquid Ar surface, saturated vapor density (ρ_{sat}), latent heat (h_{fg}), and α_M of the model fluid Ar. To determine these properties, we carry out separate MD simulations at a planar liquid-gas interface of the model fluid. The simulation details are described in Sections 3.3.1 and 3.3.2. We have used the same MD simulation method in our previous work to determine α_T, α_M, ρ_{sat}, and h_{fg} of various model fluids [15,16,18,23,33–35].

3.3.1. Determination of ρ_{sat} and h_{fg}

The saturated properties of the model fluid Ar are determined using an equilibrium MD (EMD) simulation. To determine ρ_{sat} of the model liquid Ar, we place a liquid slab of 112,437 Ar atoms at the center of a simulation box and randomly insert 6486 Ne atoms on the two sides of the liquid slab, as shown in Fig. 3(a). The length of the simulation box in the x, y, and z directions is 35, 25, and 25 nm, respectively. The box size is fixed during the EMD simulation and periodic boundary conditions (PBCs) are applied in all three directions. The number of Ne atoms is determined using the density of Ne gas surrounding the liquid droplet. We equilibrate the system at a temperature of 79.2 K for 2 ns using the Nose-Hoover thermostat [36]. The equilibrium temperature is determined from the droplet temperature at QSS. After the system reaches equilibrium, a liquid Ar slab sandwiched by a gas mixture of gas Ne and saturated Ar vapor is present in the simulation box. We then turn off the thermostat and carry out an NVE simulation for 2 ns to determine the distribution of Ar density (ρ_{Ar}) along the x-direction, as shown in Fig. 3(b). From the ρ_{Ar} at the center of the liquid slab and in the gas phase, we find the liquid density ρ_L and the saturated vapor density ρ_{sat}, respectively.

To find the latent heat, h_{fg}, of Ar at the given temperature $T_L = 79.2$ K, we perform two separate EMD simulations in a cubic simulation cell at T_L with densities set at ρ_{sat} and ρ_L, respectively. We calculate the internal energy (u), pressure (P), and enthalpy ($h = u + P\rho$) of the saturated liquid Ar and saturated vapor Ar at the given T_L. The difference between the two enthalpies gives $h_{fg} = 6.46$ kJ/mol for the model fluid Ar at $T_L = 79.2$ K. Using a similar method, we determine ρ_L, ρ_{sat}, and h_{fg} of the model fluid Ar for other cases studied in this work and summarize the simulation results in Table 2.

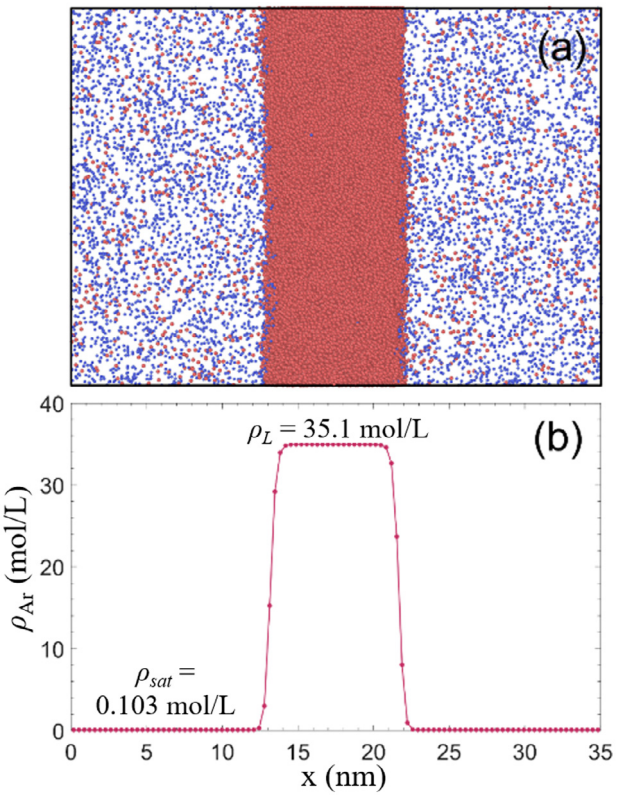

Fig. 3. (a) A snapshot of the EMD system used to determine the saturated density of model Ar. (b) The density profile in the EMD system at T = 79.2 K and P_{Ne} = 4 atm.

Table 2
Saturated properties and mass accommodation coefficient, α_M, of model fluid Ar, and thermal accommodation coefficient, α_T, of Ne gas on liquid Ar.

Case #	P_{Ne} (atm)	r_g (nm)	T_L (K)	ρ_{sat} (mol/L)	ρ_L (mol/L)	h_{fg} (kJ/mol)	α_M	α_T
1	2	110	73.6	0.047	35.9	6.61	0.95	0.89
2	4	110	79.2	0.103	35.1	6.46	0.92	0.89
3	8	110	84.9	0.199	34.2	6.30	0.87	0.87
4	4	200	79.6	0.109	35.0	6.42	0.92	0.88

3.3.2. Determination of α_T and α_M

The MD setup used to find α_M is depicted in Fig. 4(a). The system comprises of two Au plates at each end of the simulation cell. Each plate is formed by three (100) oriented Au atomic layers and a cross-sectional area of 7.75 by 7.75 nm. The outermost layer of each of the Au plates stays fixed in the simulation. We place a liquid Ar layer with an initial thickness of 6 nm on each of the two inner surfaces of the Au plates. The initial thickness of the liquid Ar slabs was selected to avoid disjoining pressure effects on the equilibrium properties of fluid Ar [15]. The distance between the two liquid surfaces is around 64 nm. We randomly insert Ne atoms into the region between the two liquid surfaces with a density close to the Ne gas near the evaporating droplet surface at QSS. All fluid-fluid and fluid-solid interactions are described by the truncated and shifted LJ potential with parameters given in Table 1, and the Au-Au interactions are described using the embedded atom method [37]. PBCs are applied in the y and z directions.

The α_M is the probability that a vapor molecule will accommodate to the liquid phase after striking the liquid surface [6,7]. Using the setup in Fig. 4(a), we set the temperature of both Au plates to 79.2 K by velocity rescaling. We equilibrate the system for 5 ns and run the EMD simulation for an additional 20 ns for data collection and averaging. We set an imaginary plane at 10.9 Å (i.e., cutoff distance) from the liquid-gas interface where the density of Ar is equal to half the liquid density. This imaginary plane helps classify atoms crossing towards the liquid surface as incident and atoms crossing in the opposite direction as reflected. We conducted five independent runs with varying initial velocities to obtain better statistics.

To determine α_M from the model system shown in Fig. 4(a), we follow the trajectory of each incident vapor molecule to determine the time interval, Δt, for each incident molecule to cross the imaginary plane again and return to the vapor phase. The time interval, Δt, for vapor molecules directly reflected by the liquid surface should be smaller than that for vapor molecules that are first accommodated to the liquid phase and later evaporated. Therefore, we need to find a cutoff time interval, Δt_{cut}, to determine if the incident molecule was accommodated to the liquid surface. We find Δt_{cut} using the normal average velocity of an incoming Ar vapor molecule, given by [22] $v_n = \sqrt{\pi RT/2M_v}$. Using v_n, the average time it takes a directly reflected incident Ar molecule to return to the gas region is $\Delta t_{cut} \approx 13.5$ ps at T = 79.2 K. If an incident vapor molecule takes more than Δt_{cut} = 13.5 ps to return to the vapor phase, we consider that the vapor molecule is first accommodated to the liquid and later evaporated. In a 20 ns-long EMD run, we measure the total number of incident Ar molecules, N_{inc}, and the number of incident Ar molecules that return to the gas phase, N_{ref}, within Δt. Accordingly, we use $\alpha_M = 1 - N_{ref}/N_{inc}$ at Δt_{cut} = 13.5 ps to evaluate α_M of model Ar at T = 79.2 K and P_{Ne} = 4 atm as shown in Fig. 5(a). The aforementioned method actually calculates the condensation coefficient of Ar using the EMD simulation. In Schrage analysis, the condensation coefficient was assumed to be the same as the evaporation coefficient [7,38]. This assumption was verified by MD simulations of evaporation in a LJ fluid system [39,40]. It was also shown in the recent study that the evaporation coefficient in the non-equilibrium state is almost the same as that in the equilibrium state [41]. Hence, the condensation coefficient and the evaporation coefficient are both the same as the MAC determined by the EMD method in this section.

We determine α_T of Ne gas on a liquid Ar surface using a similar setup. As depicted by Fig. 4(b), we remove the liquid layer on the left Au surface and maintain the left and right Au plates at a temperature of 110 K and 79.2 K, respectively. As there is no liquid layer on the hot Au surface, evaporation on the hot surface and condensation on the cold surface will not occur at steady state. In this case, heat transfer through the system at steady state is by heat conduction only [23]. We run the NEMD simulation for 6 ns to let the system reach steady state and use an additional 20 ns for data collection and averaging. For monatomic fluids, α_T is given by [22]

$$\alpha_T = \frac{T_i - T_r}{T_i - T_s}, \tag{11}$$

where T_i and T_r are the temperature of incident and reflected gas molecules, respectively, and T_s is the temperature of the liquid surface. To reduce statistical uncertainty, we ran 16 independent runs varying in initial velocities. To find the average temperature of the incident and reflected molecules crossing the imaginary plane, we recorded their kinetic energy, KE, and divided the average KE by a factor of $2k_B$ [22], where k_B is the Boltzmann constant. In Fig 5(b), we plotted the temperature running average of both incident and reflected Ne gas molecules near the liquid Ar surface. Using the simulation data, we find $\alpha_T = 0.89$ for the model Ne gas molecules on a liquid Ar surface.

Using similar methods as described above, we determine α_T and α_M for the other three cases tested in this study and summarize the results in Table 2.

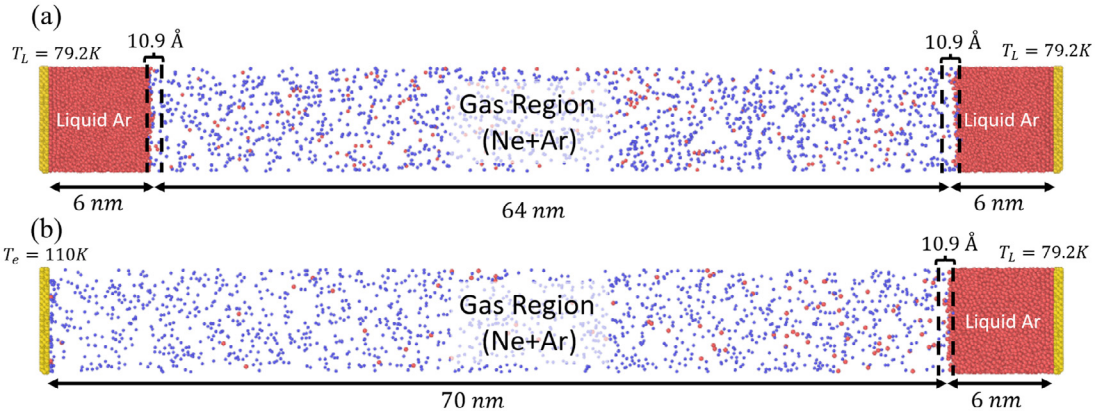

Fig. 4. (a) Snapshot of the EMD model used to determine α_M of Ar at $T = 79.2$ K and $P_{Ne} = 4$ atm. (b) Snapshot of the NEMD model used to obtain α_T of Ne gas molecules on a liquid Ar surface at $T = 79.2$ K and $P_{Ne} = 4$ atm. In both models, an imaginary plane is set at 10.9 Å from the liquid-gas interfaces to determine incident and reflected molecules used to obtain α_M and α_T.

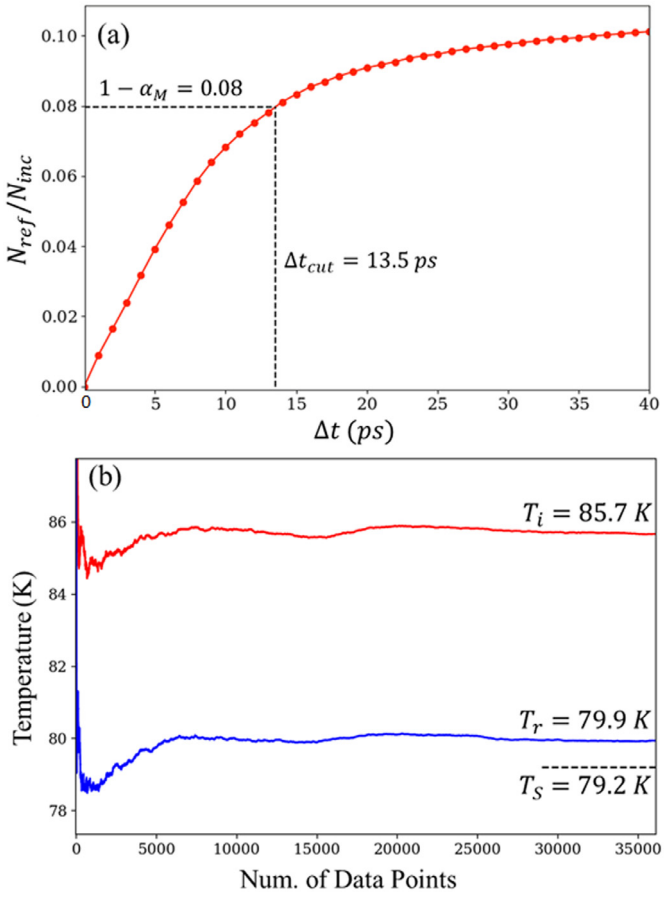

Fig. 5. (a) The ratio of reflected to incident Ar molecules, N_{ref}/N_{inc}, as a function of Δt for cases with $T = 79.2$ K and $P_{Ne} = 4$ atm. The dashed lines mark the position where α_M is evaluated at Δt_{cut}. (b) Running average of the incident and reflected Ne molecule temperatures represented by the red and blue lines, respectively.

4. Simulation results

4.1. Representative simulation results

The representative MD simulation results in the case of $P_{Ne} = 4$ atm and $r_g = 110$ nm (i.e., Case #2 in Tables 2 and 3) are shown in Fig. 6. We first use the QSS NEMD simulation results to evaluate R_K. From Fig. 2(b) we find that the droplet radius at the 30 ns-long QSS is $r_d = 26.8 \pm 1.0$ nm. At QSS, we directly find from the NEMD simulation that energy is added to the heat reservoir at a rate of $\dot{Q} = 149 \pm 7$ nW. Accordingly, q_{cond} across the liquid-gas interface is 16.5 ± 1.4 MW/m^2. At QSS, the liquid droplet temperature is essentially a constant around $T_L = 79.2$ K and heat conduction in the spherically symmetric gas phase results in a temperature profile as a linear function of $1/r$: $C - \dot{Q}_{cond}/4\pi k_g r$, where C is a fitting constant and k_g is the thermal conductivity of the gas phase [42]. As shown in Fig. 6(c), by fitting the Ne gas temperature between $r = 50$ nm and $r = 90$ nm where Ne gas and Ar vapor have almost the same temperature, we obtain $T_g = 91.7$ K and $\Delta T = 12.5$ K at the liquid-gas interface, and $k_g = 0.019$ W/m·K for the surrounding Ar-Ne gas mixture. Note the gas temperatures near the liquid-gas interface are not used in the fitting because they are within the Knudsen layer, where the gas is in a highly non-equilibrium state [14,43]. With q_{cond} and ΔT obtained from the NEMD simulation, we find $R_K = 0.76 \pm 0.06$ m^{2}K/MW from Eq. (1). To predict R_K from Eq. (2), we also fit the Ne gas density with a linear function $1/r$ as shown in Fig. 6(d) and find $\rho_g = 0.64$ mol/L at the liquid-gas interface. The Ne density near the interface is not used in the fitting because near the liquid-gas interface there is a gas adsorption layer whose Ne density is much higher than that in the gas phase [26]. With the ρ_g, T_g, and α_T obtained from MD simulations and $c_V = 1.5R$ for the model Ne gas, we obtain the theoretical prediction $R_K = 0.76$ m^{2}K/MW, which agrees with the direct MD simulation result very well.

Next, we evaluate R_M from the MD simulation results. As shown in Fig. 6(b), the molar flow rate of Ar in the gas phase is essentially a constant ($\dot{M}_{Ar} = 22.8 \pm 0.1$ pmol/s) at QSS. Using $\dot{M}_{Ar}$, r_d, and $h_{fg} = 6.46$ kJ/mol, one can easily find $J_{evp} = 2.53 \pm 0.19$ kmol/m^{2}s and $q_{evp} = 16.3 \pm 1.2$ MW/m^2 at the liquid-gas interface. $q_{evp} \approx q_{cond}$ further verifies that it is a QSS heating and evaporation process. Using the analogy between heat conduction and mass diffusion, we also fit the Ar vapor density out of the highly non-equilibrium Knudsen layer with a linear function of $1/r$ (i.e., $C + \dot{M}_{Ar}/4\pi D_{AB} r$, where D_{AB} is the binary diffusion coefficient in the Ar-Ne gas mixture) as shown in Fig. 6(d) and obtain $\rho_v = 64$ mol/m^3 at the liquid-gas interface and $D_{AB} = 0.80 \times 10^{-6}$ m^2/s. The vapor density within the Knudsen layer is not used in the fitting because the Fick's law of mass diffusion is invalid in the Knudsen layer. ρ_v is lower than $\rho_{sat}(T_L)$ by 39 mol/m^3. Accordingly, we find from Eq. (5) that $R_M = \Delta\rho/J_{evp} = 0.0154 \pm 0.0012$ s/m. From the MD simulations and the above analysis, we already know T_L, ρ_{sat}, h_{fg}, and R_K. Substituting these values and $\alpha_M = 0.92$ into Eq. (9), we find the first and second terms on right side of Eq. (9) are

Table 3
Properties of model fluids and comparison of R_K and R_M obtained directly from MD simulations with the theoretical (Th) predictions from Eq. (2) and Eq. (9), respectively. r_d is the average droplet radius at QSS.

Case #	r_d (nm)	T_g (K)	ρ_g (mol/L)	ΔT (K)	$\dot{Q}_{cond}$ (nW)	R_K (m^{2}K/MW)		ρ_v (mol/m^3)	$\Delta\rho$	J_{evp} (kmol/m^{2}s)	R_M (s/m)	
						MD	Th				MD	Th
1	26.4	91.4	0.32	17.8	105	1.48	1.52	24	23	1.78	0.013	0.014
2	26.8	91.7	0.64	12.5	149	0.76	0.76	64	39	2.53	0.015	0.015
3	25.3	91.9	1.27	7.0	155	0.36	0.40	149	50	3.12	0.016	0.015
4	26.0	92.0	0.64	12.4	137	0.77	0.77	69	40	2.48	0.016	0.015

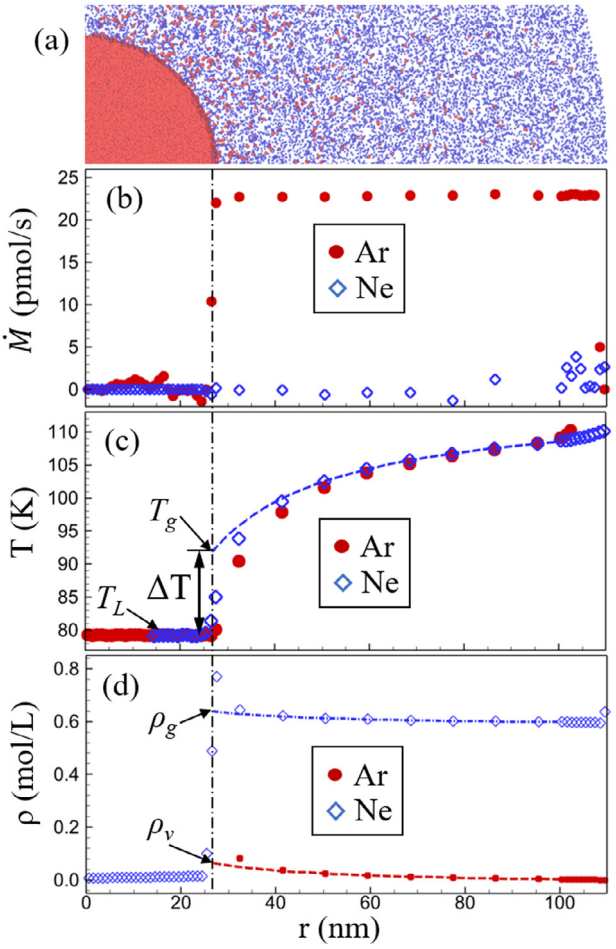

Fig. 6. (a) A snapshot of a portion of model system with initial P_{Ne} = 4 atm, and distributions of (b) molar flow rate, (c) temperature, and (d) density of Ar and Ne at QSS. The vertical line indicates the position of the liquid-gas interface. The dash line in (c) is a fit to gas Ne temperature. The dash-dot and dash lines in (d) are the fit to gas Ne and vapor Ar density, respectively. In all cases, we fitted a linear function of $1/r$ to data between r = 50 nm and r = 90 nm. The uncertainties are smaller than or comparable to the symbol size.

0.0115 s/m and 0.0032 s/m, respectively. Accordingly, Eq. (9) predicts R_M = 0.0147 s/m which agrees with the direct MD simulation result very well.

4.2. Dependence of R_K and R_M on P_{Ne} and r_g

To further test the accuracy of Eqs. (2) and (9), we extend the study of the MD model to the cases where the equilibrium P_{Ne} equals 2 atm (Case #1) and 8 atm (Case #3), respectively. As shown in Table 3, the NCG density ρ_g near the droplet surface is almost proportional to P_{Ne}, which indicates the model Ne gas can be well approximated as an ideal gas. As ρ_g increases, the rate of gas-liquid collisions and the rate of heat exchange between the droplet and the surrounding NCG increase. Eq. (2) shows R_K at the liquid-gas interface is inversely proportional to the liquid-gas collision rate N_g. Hence, it is reasonable to see in Table 3 that R_K is almost inversely proportional to P_{Ne}. As R_K decreases with increasing P_{Ne}, the heat conduction rate $\dot{Q}_{cond}$ from the surrounding NCG to the droplet increases, which heats up the droplet to a higher T_L at QSS as shown in Tables 2 and 3. As T_L increases from 73.6 K to 84.9 K, Table 2 shows the saturated vapor density ρ_{sat} of the model fluid increases by more than a factor of four and h_{fg} remain largely the same. Since the change in T_L is not significant as P_{Ne} increases and Eq. (9) shows R_M depends on the product of ρ_{sat}, h_{fg}, and R_K, it is reasonable to see in Table 3 that the interfacial mass transfer resistance R_M is not sensitive to the change in the surrounding gas pressure in the model fluid system.

Furthermore, we increase the radius r_g of the simulation cell from 110 nm to 200 nm and maintain initial P_{Ne} at 4 atm (Case #4) to study the effects of the simulation box size on R_K and R_M. The conduction resistance in the surrounding gas of the model system is [42]

$$R_g = \frac{1/r_d - 1/r_g}{4\pi k_g}. \tag{12}$$

Since r_d in the model system is more than four times smaller than r_g, increasing r_g from 110 nm to 200 nm only slightly increases the thermal resistance R_g in the surrounding gas. As a result, Tables 2 and 3 shows that as r_g increases from 110 nm to 200 nm, $\dot{Q}_{cond}$ slightly decreases, and the temperature and density of fluids near the liquid-gas interface and R_K and R_M remain almost the same.

For all cases studied in this work, the theoretical predictions of R_K and R_M from Eqs. (2) and (9) are in good agreement with those obtained directly from the NEMD simulations as shown in Table 3. In deriving Eq. (9), we assumed a small $\Delta T/T_L$. One can see from Tables 2 and 3 that the largest $\Delta T/T_L$ studied in this work is 0.24 in the case of P_{Ne} = 2 atm. In the Taylor expansion of the square root in the bracket of Eq. (7), the first high order term neglected in Eq. (8) is $(\Delta T/T_L)^2/8$ which is only 6% of $\Delta T/2T_L$ in Eq. (8) when $\Delta T/T_L$ = 0.24. Hence, it is reasonable to see that Eq. (9) can still give a good prediction of R_M when $\Delta T/T_L$ is as high as 0.24.

5. Effects of R_K and R_M on continuum modeling

Now we discuss how R_K and R_M at the liquid-gas interface affect the temperature and density boundary conditions in continuum modeling of QSS evaporation of a liquid droplet in a NCG. From the theoretical analysis in Section 2.1, we have $q_{evp} = q_{cond}$ at QSS. Using the thermal resistance network shown in Fig. 1, we obtain:

$$-h_{fg}\rho_L \frac{dV_L}{dt} = \frac{T_e - T_L}{R_g + R_K/4\pi r_d^2}, \tag{13}$$

where V_L is the volume of the liquid droplet. Note in Eq. (13) the unit of interfacial thermal resistance R_K is different from that of R_g in the surrounding gas phase. To determine whether ΔT and

R_K at an evaporating droplet surface can be neglected in the continuum modeling, one needs to know if the ratio $R_K/(R_g 4\pi {r_d}^2)$ is negligible. We consider the evaporation of a liquid droplet in an infinitely large and stagnant NCG medium. From Eq. (12), $R_g 4\pi {r_d}^2$ in an infinitely large NCG (i.e., $r_g \to \infty$) surrounding the nanodroplet is r_d/k_g. Accordingly, if the ratio $R_K k_g/r_d$ is much less than 1, ΔT at the liquid-gas interface is negligible and it is valid to assume a continuous temperature profile across the liquid-gas interface. For the representative case (i.e., Case #2) studied in this work, we find in Section 4.1 that $k_g = 0.019$ W/m·K and $R_K = 0.76$ m^{2}K/MW for $P_{Ne} = 4$ atm. Accordingly, $R_K k_g \approx 14.4$ nm, which is significant compared to $r_d \approx 26.8$ nm in our model system. Hence, ΔT at the interface is only negligible if the model droplet size increases to 1 μm or above.

To further demonstrate the importance of considering R_K in continuum modeling of evaporation of nanodroplets, we substitute Eq. (12) into Eq. (13) and obtain

$$\frac{d(r_d)}{dt} = \frac{(T_L - T_e)/\rho_L h_{fg}}{\frac{r_d}{k_g}\left(1 - \frac{r_d}{r_g}\right) + R_K}. \tag{14}$$

For the representative case studied in this work, the QSS starts at $t = 30$ ns. At QSS, the values of T_L, T_e, ρ_L, h_{fg}, r_g, k_g and R_K on right side of Eq. (14) are constant and given in Tables 2 and 3. Using numerical integration of Eq. (14), we obtain r_d vs. t of the representative case at QSS. As shown in Fig. 2(b), neglecting R_K in the continuum modeling significantly overestimates the evaporation rate of the nanodroplet. Once the KTG prediction (i.e., Eq. (2)) $R_K = 0.76$ m^{2}K/MW is taken into account, the prediction from Eq. (14) agrees with the direct MD simulation results very well as shown in Fig. 2(b). The good agreement also indicates Eq. (2) gives an accurate prediction of R_K at the liquid-gas interface of an evaporating droplet in a NCG.

Similarly, whether the approximation of saturated vapor at an evaporating nanodroplet surface is valid in the continuum modeling depends on the ratio of $R_M/4\pi {r_d}^2$ to the mass diffusion resistance in the surrounding gas phase. Using the analogy between heat conduction and mass diffusion, we obtain the diffusion resistance from the droplet surface to the infinitely large NCG is $1/4\pi D_{AB} r_d$. Accordingly, the saturated vapor assumption is valid if the ratio $R_M D_{AB}/r_d$ is much less than 1. For the representative case studied in this work, we find in Section 4.1 that $D_{AB} = 0.80 \times 10^{-6}$ m^2/s and $R_M = 0.015$ s/m for the model fluid. Accordingly, $R_M D_{AB} \approx 12$ nm, which is also significant compared to $r_d \approx 27$ nm. Hence, the saturated vapor approximation is not valid for our model nanodroplet but will be valid if r_d is greater than 1 μm.

6. Conclusions

From the study of an evaporating nanodroplet in a NCG we find that the temperature jump ΔT at the liquid-gas interface is induced by the interfacial thermal conduction resistance (R_K) and the density jump $\Delta\rho = \rho_{sat}(T_L) - \rho_v$ is induced by the resistance to the mass transfer (evaporation) across the interface (R_M). R_K and R_M can be well predicted by Eq. (2) and Eq. (9), respectively. The conventional assumptions of a continuous temperature profile and saturated vapor at the liquid-gas interface are only valid when the droplet size is significantly greater than $R_K k_g$ and $R_M D_{AB}$. If the resistance to the heat and mass flow across a liquid-gas interface of an evaporating droplet is significant compared to that in the surrounding gas, neglecting R_K and R_M at the interface could significantly overestimate the evaporation rate of the liquid droplet.

All the analysis in this work is based on MD simulation results in a model fluid mixture of Ar and Ne. While we expect that the results are general, it is imperative in the future to also investigate if the conclusions drawn in this work can be applied to systems with complex fluids such as evaporation of a water droplet in air.

Data availability

The data that support the findings of this study and the job script for MD simulations in this work are available from the corresponding author upon reasonable request.

Declaration of Competing Interest

There is no conflict of interest.

CRediT authorship contribution statement

Jesus Gutierrez Plascencia: Methodology, Writing – original draft. **Eric Bird:** Methodology, Writing – original draft. **Zhi Liang:** Conceptualization, Writing – review & editing.

Acknowledgment

This work was supported by NSF CBET Thermal Transport Processes Program under Grant No. 1911433. We would like to thank the eXtreme Science and Engineering Discovery Environment (XSEDE) for providing us supercomputer resources for MD simulations. J.G.P. would like to thank the support by the CSU-LSAMP Bridge to Doctorate program under the NSF Grant No. HRD-1905148. Any opinions, findings, and conclusions or recommendations expressed in this material are those of the author(s) and do not necessarily reflect the views of the National Science Foundation.

References

[1] M. Chaker, C.B. Meher-Homji, Gas turbine power augmentation: parametric study relating to fog droplet size and its influence on evaporative efficiency, J. Eng. Gas Turbines Power. 133 (2011) 357–369.
[2] R. Tao, K. Huang, H. Tang, D. Bell, Electrorheology leads to efficient combustion, Energy Fuels 22 (2008) 3785–3788.
[3] T. Lim, S. Han, J. Chung, J.T. Chung, S. Ko, C.P. Grigoropoulos, Experimental study on spreading and evaporation of inkjet printed pico-liter droplet on a heated substrate, Int. J. Heat Mass Transf. 52 (2009) 431–441.
[4] J.U. Park, M. Hardy, S.J. Kang, K. Barton, K. Adair, D. kishore Mukhopadhyay, C.Y. Lee, M.S. Strano, A.G. Alleyne, J.G. Georgiadis, P.M. Ferreira, J.A. Rogers, High-resolution electrohydrodynamic jet printing, Nat. Mater. 6 (2007) 782–789.
[5] G. Fang, C.A. Ward, Temperature measured close to the interface of an evaporating liquid, Phys. Rev. E 59 (1999) 417–428.
[6] A.J.H. McGaughey, C.A. Ward, Temperature discontinuity at the surface of an evaporating droplet, J. Appl. Phys. 91 (2002) 6406–6415.
[7] A.H. Persad, C.A. Ward, Expressions for the evaporation and condensation coefficients in the Hertz-Knudsen relation, Chem. Rev. 116 (2016) 7727–7767.
[8] R. Hołyst, M. Litniewski, Heat transfer at the nanoscale: evaporation of nanodroplets, Phys. Rev. Lett. 100 (2008) 055701.
[9] R. Hołyst, M. Litniewski, D. Jakubczyk, K. Kolwas, M. Kolwas, K. Kowalski, S. Migacz, S. Palesa, M. Zientara, Evaporation of freely suspended single droplets: experimental, theoretical and computational simulations, Rep. Prog. Phys. 76 (2013) 034601.
[10] R. Hołyst, M. Litniewski, D. Jakubczyk, M. Zientara, M. Woźniak, Nanoscale transport of energy and mass flux during evaporation of liquid droplets into inert gas: computer simulations and experiments, Soft Matter 9 (2013) 7766–7774.
[11] S.S. Sazhin, Advanced models of fuel droplet heating and evaporation, Prog. Energy Combust. Sci. 32 (2006) 162–214.
[12] U. Fritsching, Spray Simulation, Cambridge University Press, Cambridge, England, 2004.
[13] S. Semenov, V.M. Starov, M.G. Velarde, R.G. Rubio, Droplets evaporation: problems and solutions, Eur. Phys. J. Spec. Top. 197 (2011) 265–278.
[14] Z. Lu, I. Kinefuchi, K.L. Wilke, G. Vaartstra, E.N. Wang, A unified relationship for evaporation kinetics at low Mach numbers, Nat. Commun. 10 (2019) 2368.
[15] Z. Liang, T. Biben, P. Keblinski, Molecular simulation of steady-state evaporation and condensation: validity of the Schrage relationships, Int. J. Heat Mass Transf. 114 (2017) 105–114.
[16] Z. Liang, P. Keblinski, Molecular simulation of steady-state evaporation and condensation in the presence of a non-condensable gas, J. Chem. Phys. 148 (2018) 064708.

[17] A. Chandra, P. Keblinski, Investigating the validity of Schrage relationships for water using molecular dynamics simulations, J. Chem. Phys. 153 (2020) 124505.
[18] E. Bird, J. Gutierrez Plascencia, Z. Liang, Thermal transport across the interface between liquid n-dodecane and its own vapor: a molecular dynamics study, J. Chem. Phys. 152 (2020) 184701.
[19] E.S. Landry, S. Mikkilineni, M. Paharia, A.J.H. McGaughey, Droplet evaporation: a molecular dynamics investigation, J. Appl. Phys. 102 (2007) 124301.
[20] E.T. Swartz, R.O. Pohl, Thermal boundary resistance, Rev. Mod. Phys. 61 (1989) 605–668.
[21] J.B. Young, The condensation and evaporation of liquid droplets in a pure vapour at arbitrary Knudsen number, Int. J. Heat Mass Transf. 34 (1991) 1649–1661.
[22] F.O. Goodman, in: Dynamics of Gas-Surface Scattering, Academic Press, New York, 1976, pp. 23–31.
[23] J. Gonzalez, J. Ortega, Z. Liang, Prediction of thermal conductance at liquid-gas interfaces using molecular dynamics simulations, Int. J. Heat Mass Transf. 126 (2018) 1183–1192.
[24] P.L. Barclay, J.R. Lukes, Curvature dependence of the mass accommodation coefficient, Langmuir 35 (2019) 6196–6202.
[25] R. von Helmholtz, Untersuchungen über Dämpfe und Nebel, besonders über solche von Lösungen, Ann. Phys. 263 (1886) 508–543.
[26] E. Bird, J. Zhou, Z. Liang, Coalescence speed of two equal-sized nanobubbles, Phys. Fluids 32 (2020) 123304.
[27] G. Maitland, M. Rigby, E.B. Smith, W.A. Wakeham, Intermolecular Forces: their Origin and Determination, Clarendon Press, Oxford, 1981.
[28] D. Frenkel, B. Smit, Understanding Molecular Simulation, Academic Press, San Diego, 2002.
[29] S. Plimpton, Fast parallel algorithms for short-range molecular dynamics, J. Comput. Phys. 117 (1995) 1–19.
[30] H.J.C. Berendsen, J.P.M. Postma, W.F. van Gunsteren, A. DiNola, J.R. Haak, Molecular dynamics with coupling to an external bath, J. Chem. Phys. 81 (1984) 3684–3690.
[31] V.V. Zhakhovsky, A.P. Kryukov, V.Y. Levashov, I.N. Shishkova, S.I. Anisimov, Mass and heat transfer between evaporation and condensation surfaces: atomistic simulation and solution of Boltzmann kinetic equation, Proc. Natl. Acad. Sci. 116 (2018) 18209–18217.
[32] E. Bird, Z. Liang, Maximum evaporating flux of molecular fluids from a planar liquid surface, Phys. Rev. E 102 (2020) 043102.
[33] E. Bird, J. Gutierrez Plascencia, P. Keblinski, Z. Liang, Molecular simulation of steady-state evaporation and condensation of water in air, Int. J. Heat Mass Transf. 184 (2022) 122285.
[34] Z. Liang, K. Sasikumar, P. Keblinski, Liquid phase stability under an extreme temperature gradient, Phys. Rev. Lett. 111 (2013) 225701.
[35] E. Bird, E. Smith, Z. Liang, Coalescence characteristics of bulk nanobubbles in water: a molecular dynamics study coupled with theoretical analysis, Phys. Rev. Fluids 6 (2021) 093604.
[36] D.J. Evans, B.L. Holian, The Nose-Hoover thermostat, J. Chem. Phys. 83 (1985) 4069–4074.
[37] S.M. Foiles, M.I. Baskes, M.S. Daw, Embedded-atom-method functions for the fcc metals Cu, Ag, Au, Ni, Pd, Pt, and their alloys, Phys. Rev. B 33 (1986) 7983–7991.
[38] R.W. Schrage, A Theoretical Study of Interphase Mass Transfer, Columbia University Press, Ney York, 1953.
[39] M. Kon, K. Kobayashi, M. Watanabe, Method of determining kinetic boundary conditions in net evaporation/condensation, Phys. Fluids 26 (2014) 072003.
[40] K. Kobayasji, K. Sasaki, K. Kon, H. Fujii, M. Watanabe, Kinetic boundary conditions for vapor-gas binary mixture, Microfluid. Nanofluid. 21 (2017) 53.
[41] H. Tabe, K. Kobayashi, H. Fujii, M. Watanabe, Molecular dynamics simulation of evaporation coefficient of vapor molecules during steady net evaporation in binary mixture system, Int. J. Heat Mass Transf. 188 (2022) 122663.
[42] Y.A. Cengel, A.J. Ghajar, Heat and Mass Transfer Fundamentals & Applications, 5th ed., McGraw Hill Education, 2014.
[43] M. Knudsen, Die maximale Verdampfungsgeschwindigkeit des Quecksilbers, Ann. Phys. 352 (1915) 697–708.